Ab initio structure determination of $Cu_{2-x}Te$ plasmonic nanocrystals by precession-assisted electron diffraction tomography and HAADF-STEM imaging

Enrico Mugnaioli[a], Mauro Gemmi[a], Renyong Tu[b,c], Jeremy David[a,d], Giovanni Bertoni[b,e], Roberto Gaspari[b], Luca De Trizio[b], Liberato Manna[b]

[a] Center for Nanotechnology Innovation@NEST, Istituto Italiano di Tecnologia (IIT), Piazza San Silvestro12, 56127 Pisa, Italy

[b] Department of Nanochemstry, Istituto Italiano di Tecnologia (IIT), via Morego 30, 16163 Genova, Italy

[c] Department of Chemistry, Tsinghua University, Beijing 100084, China

[d] Catalan Institute of Nanoscience and Nanotechnology (ICN2), CSIC and BIST, Campus UAB, Bellaterra, 08193 Barcelona, Spain

[e] IMEM – CNR, Institute of Materials for Electronics and Magnetism, Parco Area delle Scienze 37/A, I-43124 Parma, Italy

Abstract

We investigated pseudo-cubic $Cu_{2-x}Te$ nanosheets using electron diffraction tomography and high-resolution HAADF-STEM imaging. The structure of this metastable nanomaterial, which has a strong localized surface plasmon resonance in the near-infrared region, was determined *ab initio* by 3D electron diffraction data recorded in low-dose nano-beam precession mode, using a new generation background-free single-electron detector. The presence of two different, crystallographically defined modulations creates a 3D connected vacancy channel system, which accounts for the strong plasmonic response of this material. Moreover, a pervasive rotational twinning is observed for nanosheets as thin as 40 nm, originating a tetragonal pseudo-symmetry.

Introduction

Over the past few years, vacancy-doped semiconducting nanocrystals (NCs), such as copper chalcogenides, have generated much interest on account of their tunable plasmonic properties[1-3]. In $Cu_{2-x}E$ (E = S, Se Te) NCs, copper vacancies lead to an increase in the charge carrier density (up to 10^{21} cm^{-3}), which results in a strong localized surface plasmon resonance (LSPR) in the near-infrared (NIR) region[4-7]. The possibility to modify the charge carrier density, and thus the LSPR, makes these materials interesting candidates for several applications in photocatalysis[8-10], photothermal therapy[11-12] and biomedical sensing[13-16].

From a practical point of view, LSPR in $Cu_{2-x}E$ NCs can be tuned by chemically controlling the copper vacancy density, which, in turn, might result in phase modifications[17-20]. Indeed, $Cu_{2-x}S$, $Cu_{2-x}Se$ and $Cu_{2-x}Te$ materials appear in many different crystalline forms[3], and a detailed characterization

of the related structures is crucial in order to understand the associated plasmonic response. Both $Cu_{2-x}S$ and $Cu_{2-x}Se$ systems have been thoroughly investigated, and a fine control over their phase transitions as well as their NC size and shape is now possible[4,21-28]. However, there have been far fewer reports on $Cu_{2-x}Te$ systems, which are characterized by an extremely complex phase diagram[19-20]. Furthermore, the synthesis of $Cu_{2-x}Te$ NCs is particularly challenging due to the reduced number of available tellurium sources[8,29-34].

Among the reported $Cu_{2-x}Te$ materials, the NCs obtained by Li et al.[8] are of particular interest because they are characterized by an intense LSPR in the NIR centered at ~900nm, which was exploited for either sensing or hyperthermia applications. Interestingly, such NCs were found to be heavily sub-stoichiometric in copper, with a mean Cu:Te ratio of about 1.5, and they crystallized in a metastable pseudo-cubic phase, which had not been previously observed for bulk materials (in the following sections we will refer to this phase as '$Cu_{1.5}Te$', even if the formula is not intended to be properly stoichiometric). On the basis of the HRTEM analysis, Li et al.[8] tentatively assigned a tetragonal cell to the $Cu_{1.5}Te$ phase, with the parameters $a = b = 7.50(5)$ Å and $c = 7.65(5)$ Å. The same authors also acknowledged that $Cu_{1.5}Te$ NCs display satellite reflections that are consistent with a superstructure with a periodicity of three unit cells (modulation-3), which they associated to an internal ordering of copper vacancies.

Later, our group[1] analyzed similar NCs, and we showed that the pseudo-cubic $Cu_{1.5}Te$ phase can be better described as an orthorhombic cell with the parameters $a = 7.50$ Å, $b = 7.53$ Å and $c = 7.48$ Å. In the same report, we also identified a more complex superstructure involving three modulations 3 x 3 x 4 (two modulation-3 and one modulation-4), which arise along the three main orthorhombic directions. More recently, Willhammar et al.[35] carried on the structural characterization of this material, combining aberration-corrected HAADF-STEM imaging and related 3D tomographic reconstructions with 3D electron diffraction. Based on electron diffraction data, they determined *ab initio* the structure of the non-modulated simplified cubic cell in the *Pm*-3*n* space group, therefore they did not consider any of the observed modulations or related satellite reflections, which, in turn, contain the crystallographic information about the vacancy ordering. The HAADF-STEM images clearly displayed the modulation-4, but they were not conclusive with regard to the modulations-3 that had been previously reported by other authors[1,8]. Eventually, Willhammer et al.[35] proposed a structural model which comprised only the modulation-4, in which vacancy positions could be only tentatively assigned on the basis of the 3D tomographic reconstruction.

The difficulty in crystallographically addressing the pseudo-cubic $Cu_{1.5}Te$ phase arises as a result of the small NC size and the intrinsic complexity of the structure. Such difficulties are not specific of the $Cu_{2-x}Te$ system; indeed, they are rather common in functional nanomaterials, since the properties of interest may be triggered by unusual structural features. Due to the reduced crystal size, conventional X-ray single-crystal methods are not suitable. X-ray powder diffraction (XRPD) is often not sufficient for achieving an *ab initio* structure determination for two main reasons: the crystallographic information is projected in one dimension, with a systematic or random overlap of independent crystallographic reflections; the small size of NC results in a marked broadening of the peak profiles. XRPD interpretation then becomes problematic when more crystalline phases are present in the same experimental yield[36].

Accelerated electrons can instead be focused on single particles or volumes that are less than one micron in size. Indeed, high-resolution TEM imaging techniques, such as aberration-corrected HRTEM and HAADF-STEM, are extremely powerful for the characterization of fine local structural details, like surface asperities, grain boundaries, single defects and even single atom mobilization[37]. However, imaging techniques are usually not able to deliver *ab initio* the 3D crystal structure of a new material, especially when it is characterized by large cell parameters, low symmetry and a high sensitivity to the electron beam damage[35].

On the other hand, electron diffraction has experienced a fast growth over the last few years, which is mainly connected with the introduction of 3D strategies for data collection[38-44], and this is generally referred to as electron diffraction tomography (EDT). EDT allows highly complete 3D structural data sets to be obtained from single sub-micrometric crystals, with a significant reduction in multi-scattering (dynamical effects) compared with conventional in-zone electron diffraction patterns. The whole acquisition is performed with an extremely low electron dose rate and with a total exposure time of less than one minute, and therefore it is possible to collect full data sets on extremely beam-sensitive materials. This method has been successfully exploited for the structure determination of many materials that can be synthesized only in the form of sub-micrometric crystals, ranging from complex minerals[45] to porous materials for advanced applications[46-47], highly beam-sensitive organics and hybrid compounds[48-49] and macromolecules[43,50]. EDT has been used also for the structure determination of complex intermetallic, oxide or chalcogenide NCs, even when they have been embedded in multi-phasic systems and solid matrices[51-55].

In order to obtain NCs with an optimal size for EDT measurements, we devised a new colloidal synthesis of $Cu_{2-x}Te$ nanosheets (NSs) with a composition close to $Cu_{1.5}Te$ and a lateral size up to 300 nm. NSs crystallize in the same $Cu_{1.5}Te$ metastable pseudo-cubic structure that had previously been reported for NCs[1,8,35]. Due to the relatively large lateral dimensions, EDT acquisitions could be performed with optimal settings on single NSs. EDT data were acquired in nano-beam precession-assisted mode[39,42] and recorded using a new generation MEDIPIX single-electron detector[56], which allows for an extremely low dose illumination and a considerable reduction in beam damage and contamination during data collection. Such improved data eventually enabled an *ab initio* determination of the vacancy ordering in the modulated $Cu_{2-x}Te$ structure which is responsible for both modulation-4 and modulation-3. The NSs were also discovered to be systematically affected by a rotational twinning that is connected with the particle size, which simulates a pseudo-tetragonal symmetry and is responsible for the shading of modulation-3 in TEM imaging.

Experimental Section

Materials. Copper (II) acetylacetonate ($Cu(acac)_2$, 97%), tri-n-octylphosphine (TOP, 97%), 1,2 dichlorobenzene (DCB, 99%) and octylamine (Oct, 99,5%) were purchased from Sigma-Aldrich. Tellurium powder (99.999%) was purchased from Strem Chemicals. Ethanol (anhydrous, ≥99.8%), and chloroform (anhydrous, ≥99%) were purchased from Carlo Erba reagents. All chemicals were used as received without further purification and all reactions were carried out under nitrogen using standard air-free techniques.

Synthesis of $Cu_{2-x}Te$ Nanosheets. In a typical experiment, 1 mmol of $Cu(acac)_2$, 5 mL of Oct and 5 mL of DCB were mixed together in a 25 mL three-necked flask. The flask was pumped to vacuum at room temperature for 30 min before being heated to 175 °C under N_2 flow. At this point, 2.5 mL of a 0.4 M Te-TOP precursor solution (The TOP-Te solution was obtained by dissolving tellurium powder in TOP at 150 °C for two hours) was injected and the reaction was stopped after 30 min by removing the heating mantle. The NCs were isolated by centrifugation and washed twice by re-dissolution in chloroform and precipitation with the addition of ethanol. Finally, the NCs were dispersed in chloroform and stored in a N_2 filled glove-box.

X-Ray Diffraction (XRD) measurements. The XRD analysis was performed on a PANalytical Empyrean X-ray diffractometer equipped with a 1.8 kW CuKα ceramic X-ray tube, PIXcel^{3D} 2x2 area detector operating at 45 kV and 40 mA. Specimens for the XRD measurements were prepared in a glove box by dropping a concentrated NC solution onto a quartz zero-diffraction single crystal substrate. The diffraction patterns were collected under ambient conditions using a parallel beam geometry and symmetric reflection mode. XRD data analysis was carried out using the HighScore 4.1 software from PANalytical.

Elemental Analysis. This was carried out via Inductively Coupled Plasma Atomic Emission Spectroscopy (ICP-AES), using an iCAP 6500 Thermo spectrometer. Samples were dissolved in HCl/HNO_3 3:1 (v/v). All chemical analyses performed by ICP-AES were affected by a systematic error of about 5%.

Electron diffraction tomography (EDT). EDT measurements[38,41] were performed at the Center for Nanotechnology Innovation@NEST by a Zeiss Libra TEM operating at 120 kV and equipped with a LaB_6 source and a Bruker EDS detector XFlash6T-60. EDT acquisitions were done in STEM mode after defocusing the beam in order to have a pseudo-parallel illumination on the sample. A beam size of about 150 nm in diameter was obtained by inserting a 5 μm C2 condenser aperture. An extremely mild illumination was adopted in order to avoid any alteration or amorphization of the sample, or any accumulation of organic contaminant during the EDT experiments.

EDT was performed with a processing beam[39,42,57] obtained by a Nanomegas Digistar P1000 device. The precession semi-angle was kept at 1°. Independent data sets were recorded for 10 particles, with acquisition tilt ranges up to 130° and tilt step of 1°. Camera lengths of 180 and 230 mm were used in different experiments, with an actual resolution in reciprocal space ranging from 0.75 to 1.10 Å. EDT data were recorded by an ASI Timepix detector[48,56], which was able to record the arrival of single electrons and deliver a pattern that is virtually background-free. These data were analyzed using ADT3D[41] and in-home developed MATLAB routines.

The *ab initio* structure solution was achieved using direct methods that are implemented in the software SIR2014[58]. Fourier mapping and least-squares refinement was performed using the software SHELXL[59] after imposing a soft SADI restraint on the Cu-Te and Cu-Cu distances as well as equal isotropic displacement parameters for the Te and Cu atoms, respectively. For both the *ab initio* structure determination and the structure refinement, data were treated with the kinematical approximation (I_{hkl} proportional to F^2_{hkl}), using scattering factors for electrons that are present in the SIR2014 database[60]. Since the polynomial coefficients for tellurium (Z = 52) are not present in this database, values of neighboring antimony (Z = 53) were taken for structure refinement.

HAADF-STEM images. High angle annular dark-field scanning transmission electron microscopy (HAADF-STEM) images were acquired on a JEM-ARM300F (GRAND ARM) transmission electron microscope at the JEOL Electron Microscopy Application Department (JEOL Ltd., Tokyo, Japan). The GRAND ARM is equipped with a cold field emission gun operated at 300 kV and both probe and image correctors (STEM resolution < 70 pm). The STEM convergence half-angle was approximately 22 mrad and the inner collection half-angle of the detector was >45 mrad (HAADF). STEM image simulations were carried out in the linear approximation[61] using the program STEM_CELL[62]. Energy dispersive X-ray spectroscopy (EDS) chemical maps at atomic resolution were acquired with a dual detectors system inserted in the large-gap objective pole piece.

Results and Discussion

To date, pseudo-cubic $Cu_{1.5}Te$ NCs have been reported in the form of nanocubes, nanoplateteles and nanorods that have a lateral dimension of about 20 nm[1,8]. In order to attain NCs with an optimal size for EDT measurements, we devised a new synthesis by which we could prepare NSs with a lateral dimension in the range of 50-300 nm and a thickness of less than 40 nm (**Figure 1a,b**). ICP and EDS analyses revealed both a Cu:Te ratio close to 1.40 (**Table S1**) and XRPD analysis confirmed that NSs crystallize in the metastable pseudo-cubic $Cu_{1.5}Te$ structure (**Figure S1**).

The EDT analysis revealed that all the sampled NSs have a pseudo-cubic sub-cell with an *a* around 7.5 Å. However, careful analysis revealed that the cell parameter that is orthogonal to the NS main facet (the slowest growth direction) is systematically shorter, with a value of about 7.4 Å. The smaller NSs, with a lateral size of 100-150 nm, usually have a more elongated rectangular shape and show satellite reflections that arise from two different modulations, which respectively triplicate (modulation-3) and quadruplicate (modulation-4) the cell parameters (**Figure 1c**). The modulation-4 is always orthogonal to the main NS facet and is often associated with a pronounced diffuse scattering, indicating the presence of a stacking disorder along the short NS dimension. In contrast to what was reported by Willhammer et al.[35], satellite reflections belonging to modulation-4 and modulation-3 appear equally strong here, suggesting that both features must be taken into account for a proper crystal structure characterization.

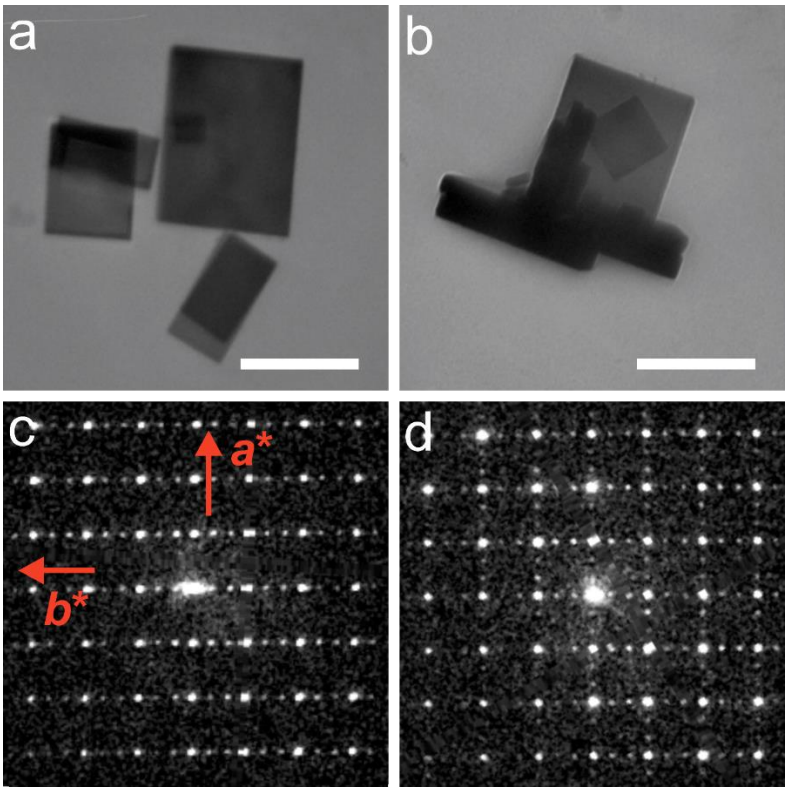

Figure 1. $Cu_{1.5}Te$ nanosheets (NS). (a) Low resolution TEM image of typical NSs lying on their large facet. Smaller NSs have generally a more elongated rectangular shape, while larger ones are more quadratic. (b) TEM image showing few $Cu_{1.5}Te$ NSs standing on side. The thickness of these NSs is around 30-40 nm. (c) Oriented [001] nano-beam diffraction pattern of a small rectangular NS, showing only one modulation-3 (crystallographic direction *b**). (d) Oriented [001] nano-beam diffraction pattern of a larger quadratic NS, showing two modulations-3 due to the pseudo-tetragonal twinning. Scale bar in (a) and (b) is 200 nm.

The larger NSs generally show a more squared morphology, and present three modulations: one modulation-4 which is orthogonal to the main facet and two modulation-3 along both the long horizontal sides (**Figure 1d**). In certain cases, the intensity of the satellite reflections that belong to the two modulations-3 appear fairly equal, giving the impression that it is tetragonally symmetric. In other cases, however, one modulation-3 is significantly stronger than the other. Having considered such intensity fluctuations and the fact that the second modulation-3 arises only in larger NSs, we infer that the $Cu_{1.5}Te$ NSs develop a pseudo-tetragonal rotational twinning along [001] above a certain critical dimension, which is responsible for the appearance of the second modulation-3. Since we observed the two modulations over the whole platelet area, it is more likely that the twin boundary is the {001} plane.

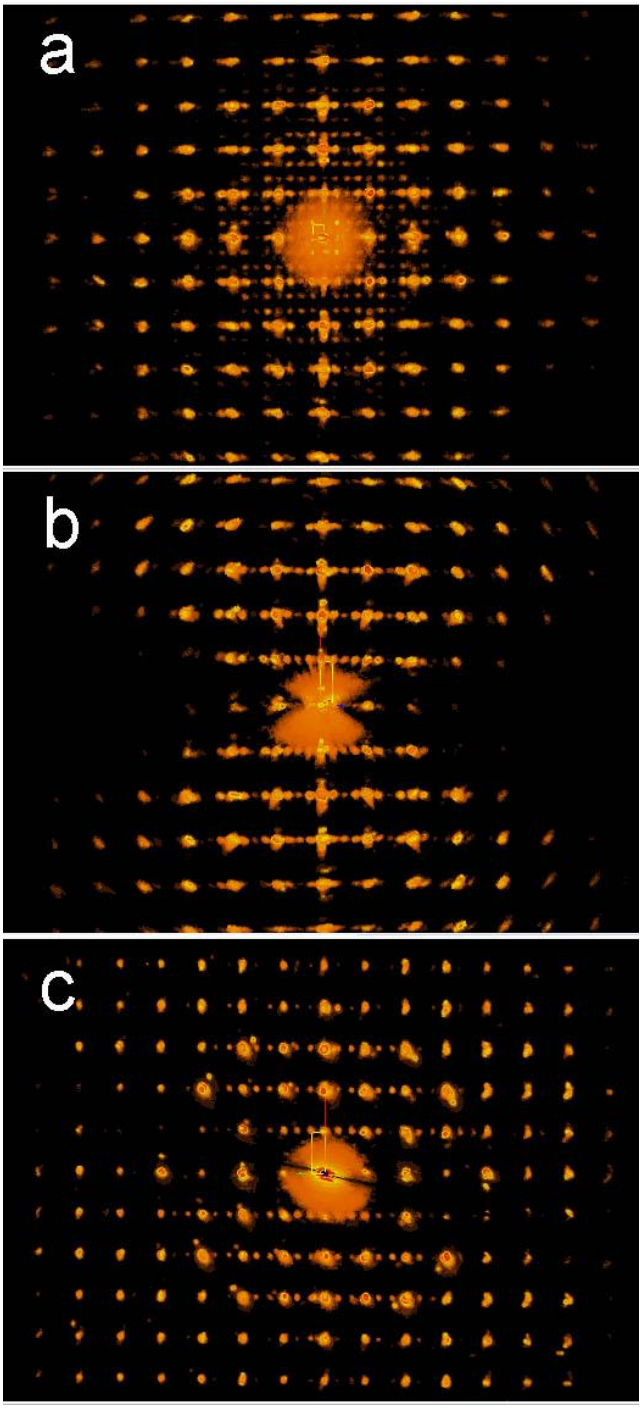

Figure 2. 3D EDT reconstructed diffraction volume for a single $Cu_{1.5}Te$ nanoparticle. (a) View along ***a**** showing both modulation-3 and modulation-4. (b) View along ***b**** showing only modulation-4. (c) View along ***c**** showing only modulation-3. Note that those are not conventional 2D oriented diffraction patterns, but projections of a 3D diffraction volume.

The final model for a non-twinned particle, therefore, involves a complex supercell which is obtained by multiplying the pseudo-cubic sub-cell by 1 x 3 x 4 (**Figure 2**). The resulting orthorhombic cell has parameters a = 7.5(1) Å, b = 22.8(2) Å, c = 29.6(3) Å, and the c direction is always orthogonal to the NS main facet. No reflection extinction was detected in the EDT data sets. It must be noted, however,

that the 00*l* reflections could not be sampled due to the NS's morphology and related preferential orientation on the TEM grid. Thus, the presence of a screw axis along *c* could not be ruled out.

The *ab initio* structure solution was eventually achieved in the acentric space group $P222_1$ (number 17). Experimental details are reported in **Table S2**. Twenty-six of the expected 27 independent Te atoms were correctly assigned using SIR2014 automatic procedures, while the last one was among the first Cu positions. Thirty-one additional maxima in the potential map were assigned to Cu atoms. As expected, all Cu atoms are tetrahedrally coordinated by four Te atoms. In total, the unit cell contains 96 Te and 124 Cu atoms, corresponding to a Cu:Te ratio of 1.29.

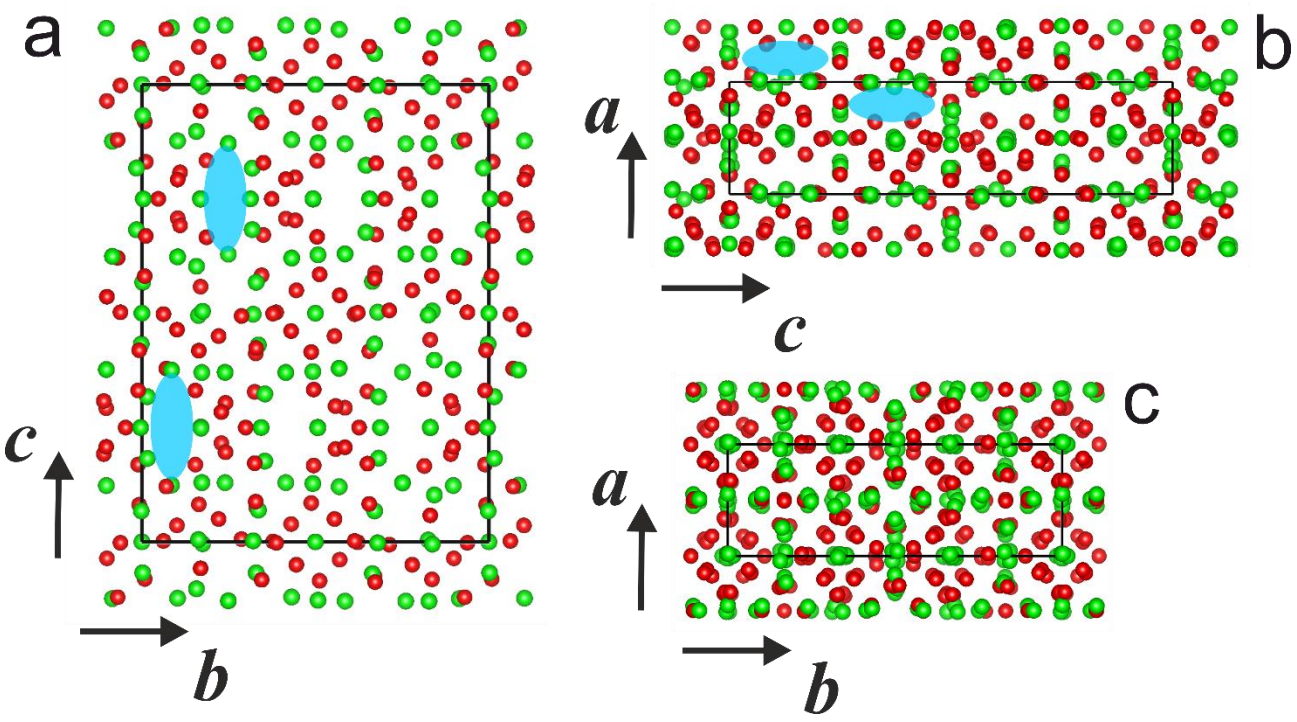

Figure 3. $Cu_{1.5}Te$ structure determined and refined by electron diffraction tomography (EDT) data. (a) View along [100], with [100] channels highlighted in blue. (b) View along [010]. Projections of low-density regions responsible for the up-up-down-down pattern in [010] HAADF-STEM images are highlighted in blue. (c) View along [001].

Soft-restrained least squares refinement resulted in a model that is very similar to the one that was derived *ab initio* (**Figure 3**). No further significant residuals were located in the difference Fourier map, but the presence of other Cu positions with a low occupancy has to be assumed in order to reach the expected Cu:Te ratio that was measured by EDS and ICP. Such positions, which are randomly distributed in the vacant tetrahedral sites of the Te-framework, could not be addressed with the available EDT data. The structure was eventually validated by the Rietveld method against XRPD data. Only the experimental parameters and cell parameters were refined, thus obtaining a reasonable fit (**Figure S1**).

The so-determined $Cu_{1.5}Te$ structure consists of a pseudo-cubic arrangement of Te atoms, which in projection, gives the impression of 3x3 centered cages. This is in agreement with the model proposed by Willhammar et al.[35]. However, less than half of the Cu positions predicted by the simplified cubic model are present. The *ab initio* model which was obtained having taken into account the satellite

reflections shows that Cu vacancies are crystallographically ordered, shaping elliptical channels that stretch along [100]. Such channels have a dimension of about 3 x 7 Å, and they are arranged in an alternating fashion along the {001} layers (**Figure 3a**). Further low-density areas develop parallel to the (100) plane, putting the former channels in communication and creating an effective 3D network of vacancies (**Figure 3b** and **Figure S2**).

Cu-Te atomic distances have an average value of 2.70(10) Å, which is in agreement with other natural and synthetic $Cu_{2-x}Te$ compounds[63-67]. Cu-Cu distances have quite scattered values, with an average of 2.58(25) Å and a minimum value of 2.03 Å. This unfeasible distance may be explained only assuming an alternated occupancy of neighboring Cu positions. However, distances down to 2.28 Å, *i.e.* shorter than Cu-Cu distances in metallic copper, have already been observed in the modulated mineral weissite ($Cu_{2-x}Te$, $x \approx 0.21$)[67] and in its synthetic analogous $Cu_{2-x}Te$ phase β^{III} [64], where they were associated with the mobility of copper ions that may appear in different valence states, *i.e.* either Cu^{+} or Cu^{2+}.

In order to further validate the *ab inito* EDT model, we acquired probe-corrected HAADF-STEM images and compared them with the corresponding simulated images (**Figure 4**). **Figure 4a**, taken along the [001] direction, shows the pseudo-cubic arrangement that has already been observed by Willhammar et al.[35]. The lower inset further displays an atomic EDS color map with the Te atoms in green and the Cu atoms in red (the individual Te-L and Cu-K maps are presented in **Figure S3**). Te and Cu sublattices are well resolved in the maps, without the need of averaging on more unit cells.

Figure 4b,c, which correspond respectively to the projections [100] and [010], show the different order of Cu vacancies, and they are consistent with the model derived by EDT. In both images, modulation-4 is immediately evident. Along [100], this modulation produces the characteristic left-right dark regions that are associated with the vacancy channels. However, along [010], modulation-4 produces a typical up-up-down-down periodicity of dark regions which has never been spotted before and which is in good agreement with the EDT derived structure.

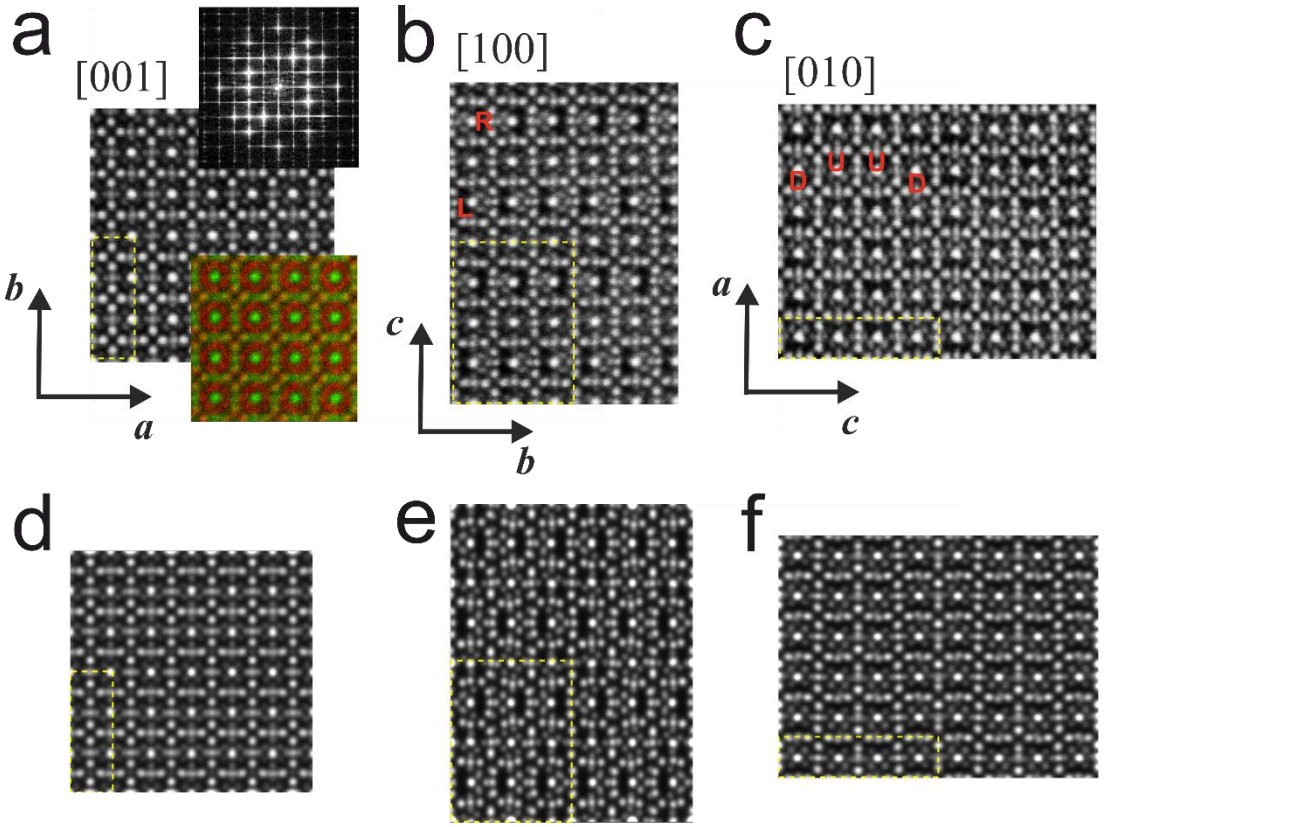

Figure 4. Experimental and simulated HAADF-STEM images of NSs. (a) Experimental image taken along [001]. The upper inset shows the corresponding FFT, where the modulation-3 is more evident. The lower inset shows the EDS chemical map at atomic resolution, where the Te sublattice (green) and the Cu sublattice (red) are straightforwardly addressed. (b) Experimental image taken along [100]. The typical left-null-right-null Cu vacancy pattern along *c* is emphasized by red labels (L and R). (c) Experimental image taken along [010]. The down-up-up-down Cu vacancy pattern along *c* is emphasized by red labels (D and U). (d) Simulated image along [001]. (e) Simulated image along [100]. (f) Simulated image along [010]. Unit cell is sketched in yellow.

Modulation-3 is expected to appear in both the [100] and [001] projections, but it can barely be identified in STEM images. Still, it clearly appears in conventional electron diffraction patterns (**Figure 1c,d**) and on the Fourier transforms of the experimental STEM images (upper inset in **Figure 4a**). This modulation is also less apparent in the simulated counterparts (**Figure 4d,f**). The presence of not low-occupied Cu sites that have not been determined and the occurrence of {001} twinned layers in the NSs may further weaken the contrast from modulation-3 and make it almost invisible in the projected potentials of the STEM images. Twinning can, in fact, already appear for very small particles, as was observed by Tu et al.[1] on nanocubes of about 20 nm.

Conclusions

$Cu_{1.5}Te$ is an example of a complex crystal structure which arises only in nanocrystalline form. It exhibits a double superstructure along two crystallographic directions of an average pseudo-cubic

cell. A conventional X-ray structural study is hampered by the sub-micrometric size of the available single crystals. Conversely, electron diffraction tomography (EDT) can provide 3D structural data on NCs of such dimensions. This technique had already been applied to $Cu_{1.5}Te$ in order to elucidate its pseudo-cubic average structure[35]. That model was partially completed by high-resolution HAADF-STEM tomographic imaging, which allowed a tentative location of vacancies, and was obtained having only considered one of the two observed modulations and without ensuing a complete atomic structure. In this paper, the structural model for the pseudo-cubic $Cu_{1.5}Te$ phase was obtained *ab initio* by 3D precession-assisted EDT data, quantitatively taking into account all observed modulations and related satellite reflection intensities. The model clearly shows an ordered crystalline arrangement of vacancies, which is consistent with the features that were observed in HAADF-STEM imaging. EDT data also evidence the presence of a rotation twinning which simulates a pseudo-tetragonal symmetry and which may already be present in very small particles, like the 20 nm nanocubes reported by Tu et al.[1] or the 40 nm thick NSs described in this paper.

The structure determination of the $Cu_{1.5}Te$ phase from single-crystal diffraction data confirms once more the effectiveness of EDT at characterizing the complex atomic structures that are often associated with nanomaterials. EDT can be easily combined with high-resolution imaging and nano-resolved chemical analysis inside the same TEM for a comprehensive structural description, enabling nanomaterials' astonishing properties to be quantitively understood.

Data availability. Details regarding the presented crystal structure are available in CIF format in the Supplementary Information.

References

1. Tu, R.; Xie, Y.; Bertoni, G.; Lak, A.; Gaspari, R.; Rapallo, A.; Cavalli, A.; De Trizio, L.; Manna, L. Influence of the Ion Coordination Number on Cation Exchange Reaction with Copper Telluride Nanocrystals. *J. Am. Chem. Soc.* **2016**, *138*, 7082–7090.
2. Kriegel, I.; Scotognella, F.; Manna, L. Plasmonic doped semiconductor nanocrystals: Properties, fabrication, applications and perspectives. *Phys. Rep.* **2017**, *674*, 1–52.
3. Agrawal, A.; Cho, S. H.; Zandi, O.; Ghosh, S.; Johns, R. W.; Milliron, D. J. Localized Surface Plasmon Resonance in Semiconductor Nanocrystals, *Chem. Rev.* **2018**, *118*, 3121–3207.
4. Zhao, Y.; Pan, H.; Lou, Y.; Qiu, X.; Zhu, J.; Burda, C. Plasmonic $Cu_{2-x}S$ Nanocrystals: Optical and Structural Properties of Copper-Deficient Copper(I) Sulfides. *J. Am. Chem. Soc.* **2009**, *131*, 4253–4261.
5. Dorfs, D.; Härtling, T.; Miszta, K.; Bigall, N. C.; Kim, M. R.; Genovese, A.; Falqui, A.; Povia, M.; Manna, L. Reversible Tunability of the Near-Infrared Valence Band Plasmon Resonance in $Cu_{2-x}Se$ Nanocrystals. *J. Am. Chem. Soc.* **2011**, *133*, 11175–11180.
6. Luther, J. M.; Jain, P. K.; Ewers, T.; Alivisatos, A. P. Localized surface plasmon resonances arising from free carriers in doped quantum dots. *Nat. Mater.* **2011**, *10*, 361–366.

7. Kriegel, I.; Jiang, C.; Rodríguez-Fernández, J.; Schaller, R. D.; Talapin, D. V.; da Como, E.; Feldmann, J. Tuning the Excitonic and Plasmonic Properties of Copper Chalcogenide Nanocrystals. *J. Am. Chem. Soc.* **2012**, *134*, 1583–1590.
8. Li, W.; Zamani, R.; Rivera Gil, P.; Pelaz, B.; Ibáñez, M.; Cadavid, D.; Shavel, A.; Alvarez-Puebla, R. A.; Parak, W. J.; Arbiol, J.; Cabot, A. CuTe Nanocrystals: Shape and Size Control, Plasmonic Properties, and Use as SERS Probes and Photothermal Agents. *J. Am. Chem. Soc.* **2013**, *135*, 7098–7101.
9. Manzi, A.; Simon, T.; Sonnleitner, C.; Döblinger, M.; Wyrwich, R.; Stern, O.; Stolarczyk, J. K.; Feldmann, J. Light-Induced Cation Exchange for Copper Sulfide Based CO_2 Reduction. *J. Am. Chem. Soc.* **2015**, *137*, 14007–14010.
10. Wang, X.; Ke, Y.; Pan, H.; Ma, K.; Xiao, Q.; Yin, D.; Wu, G.; Swihart, M. T. Cu-Deficient Plasmonic $Cu_{2-x}S$ Nanoplate Electrocatalysts for Oxygen Reduction. *ACS Catal.* **2015**, *5*, 2534–2540.
11. Hessel, C. M.; Pattani, V. P.; Rasch, M.; Panthani, M. G.; Koo, B.; Tunnell, J. W.; Korgel, B. A. Copper Selenide Nanocrystals for Photothermal Therapy. *Nano Lett.* **2011**, *11*, 2560–2566.
12. Wang, S.; Riedinger, A.; Li, H.; Fu, C.; Liu, H.; Li, L.; Liu, T.; Tan, L.; Barthel, M. J.; Pugliese, G.; De Donato, F.; Scotto D'Abbusco, M.; Meng, X.; Manna, L.; Meng, H.; Pellegrino, T. Plasmonic Copper Sulfide Nanocrystals Exhibiting Near-Infrared Photothermal and Photodynamic Therapeutic Effects. *ACS Nano* **2015**, *9*, 1788–1800.
13. Zhao, Y.; Burda, C. Development of plasmonic semiconductor nanomaterials with copper chalcogenides for a future with sustainable energy materials. *Energ. Environ. Sci.* **2012**, *5*, 5564–5576.
14. Goel, S.; Chen, F.; Cai W. Synthesis and Biomedical Applications of Copper Sulfide Nanoparticles: From Sensors to Theranostics. *Small* **2014**, *10*, 631–645.
15. Niezgoda, S.; Rosenthal, S. J. Synthetic Strategies for Semiconductor Nanocrystals Expressing Localized Surface Plasmon Resonance. *ChemPhyChem* **2016**, *17*, 645–653.
16. van der Stam, W.; Berends, A. C.; de Mello Donega, C. Prospects of Colloidal Copper Chalcogenide Nanocrystals. *ChemPhysChem* **2016**, *17*, 559–581.
17. Chakrabarti, D. J.; Laughlin, D. E. The Cu-Se (Copper-Selenium) system. *Bull. Alloy Phase Diagr.* **1981**, *2*, 305–315.
18. Chakrabarti, D. J.; Laughlin, D. E. The Cu-S (Copper-Sulfur) system. *Bull. Alloy Phase Diagr.* **1983**, *4*, 254.
19. Pashinkin, A. S.; Fedorov, V. A. Phase Equilibria in the Cu-Te System. *Inorg. Mater.* **2003**, *39*, 539–554.
20. Pashinkin, A. S.; Pavlova, L. M. *p-T* Phase Diagram of the Cu-Te System. *Inorg. Mater.* **2005**, *41*, 939–944.
21. Larsen, T. H.; Sigman, M.; Ghezelbash, A.; Doty, R. C.; Korgel, B. A. Solventless Synthesis of Copper Sulfide Nanorods by Thermolysis of a Single Source Thiolate-Derived Precursor. *J. Am. Chem. Soc.* **2003**, *125*, 5638–5639.
22. Sigman, M. B.; Ghezelbash, A.; Hanrath, T.; Saunders, A. E.; Lee, F.; Korgel, B. A. Solventless Synthesis of Monodisperse Cu_2S Nanorods, Nanodisks, and Nanoplatelets. *J. Am. Chem. Soc.* **2003**, *125*, 16050–16057.
23. Brelle, M. C.; Torres-Martinez, C. L.; McNulty, J. C.; Mehra, R. K.; Zhang, J. Z. Synthesis and characterization of Cu x S nanoparticles. Nature of the infrared band and charge-carrier dynamics. *Pure Appl. Chem.* **2000**, *72*, 101–17.

24. Wu, Y.; Wadia, C.; Ma, W.; Sadtler, B.; Alivisatos, A. P. Synthesis and Photovoltaic Application of Copper(I) Sulfide Nanocrystals. *Nano Lett.* **2008**, *8*, 2551–2555.
25. Deka, S.; Genovese, A.; Zhang, Y.; Miszta, K.; Bertoni, G.; Krahne, R.; Giannini, C.; Manna, L. Phosphine-Free Synthesis of p-Type Copper(I) Selenide Nanocrystals in Hot Coordinating Solvents. *J. Am. Chem. Soc.* **2010**, *132*, 8912–8914.
26. Li, W.; Shavel, A.; Guzman, R.; Rubio-Garcia, J.; Flox, C.; Fan, J.; Cadavid, D.; Ibáñez, M.; Arbiol, J.; Morante, J. R.; Cabot, A. Morphology evolution of $Cu_{2-x}S$ nanoparticles: from spheres to dodecahedrons. *Chem. Commun.* **2011**, *47*, 10332–10334.
27. Riha, S. C.; Johnson, D. C.; Prieto, A. L. Cu_2Se Nanoparticles with Tunable Electronic Properties Due to a Controlled Solid-State Phase Transition Driven by Copper Oxidation and Cationic Conduction. *J. Am. Chem. Soc.* **2011**, *133*, 1383–1390.
28. Kruszynska, M.; Borchert, H.; Bachmatiuk, A.; Rümmeli, M. H.; Büchner, B-, Parisi, J. and Kolny-Olesiak, J. Size and Shape Control of Colloidal Copper(I) Sulfide Nanorods. *ACS Nano* **2012**, *6*, 5889–5896.
29. Li, B.; Xie, Y.; Huang, J.; Liu, Y.; Qian, Y. Sonochemical Synthesis of Nanocrystalline Copper Tellurides Cu_7Te_4 and Cu_4Te_3 at Room Temperature. *Chem. Mater.* **2000**, *12*, 2614–2616.
30. Palchik, O.; Kerner, R. Zhu, Z.; Gedanken, A. Preparation of $Cu_{2-x}Te$ and HgTe by Using Microwave Heating. *J. Solid State Chem.* **2000**, *154*, 530–534.
31. Zhang, Y.; Qiao, Z.-P.; Chen, X.-M. Microwave-assisted elemental direct reaction route to nanocrystalline copper chalcogenides CuSe and Cu_2Te. *J. Mater. Chem.* **2002**, *12*, 2747–2748.
32. Jiang, L.; Zhu, Y.-J.; Cui J.-B. Nanostructures of Metal Tellurides (PbTe, CdTe, $CoTe_2$, Bi_2Te_3, and Cu_7Te_4) with Various Morphologies: A General Solvothermal Synthesis and Optical Properties. *Eur. J. Inorg. Chem.* **2010**, *19*, 3005–3011.
33. Kriegel, I.; Rodríguez-Fernández, J.; Wisnet, A.; Zhang, H.; Waurisch, C.; Eychmüller, A.; Dubavik, A.; Govorov, A. O.; Feldmann, J. Shedding Light on Vacancy-Doped Copper Chalcogenides: Shape-Controlled Synthesis, Optical Properties, and Modeling of Copper Telluride Nanocrystals with Near-Infrared Plasmon Resonances. *ACS Nano* **2013**, *7*, 4367–4377.
34. Li, H.; Brescia, R.; Povia, M.; Prato, M.; Bertoni, G.; Manna, L.; Moreels, I. Synthesis of Uniform Disk-Shaped Copper Telluride Nanocrystals and Cation Exchange to Cadmium Telluride Quantum Disks with Stable Red Emission. *J. Am. Chem. Soc.* **2013**, *135*, 12270–12278.
35. Willhammar, T.; Sentosun, K.; Mourdikoudis, S.; Goris, B.; Kurttepeli, M.; Bercx, M.; Lamoen, D.; Partoens, B.; Pastoriza-Santos, I.; Pérez-Juste, J.; Liz-Marzán, L. M.; Bals, S.; Van Tandeloo G. Structure and vacancy distribution in copper telluride nanoparticles influence plasmonic activity in the near-infrared. *Nat. Commun.* **2017**, *8*, 14925.
36. Yun, Y.; Zou, X.; Hovmöller, S.; Wan, W. Three-dimensional electron diffraction as a complementary technique to powder X-ray diffraction for phase identification and structure solution of powders. *IUCrJ* **2015**, *2*, 267–282.
37. LeBeau, J. M.; Findlay, S. C.; Allen, L. J.; Stemmer, S. Standardless Atom Counting in Scanning Transmission Electron Microscopy. *Nano Lett.* **2010**, *10*, 4406–4408.
38. Kolb, U.; Gorelik, T.; Kübel, C.; Otten, M. T.; Hubert, D. Towards automated diffraction tomography: Part I—Data acquisition. *Ultramicroscopy* **2007**, *107*, 507–513.

39. Mugnaioli. E.; Gorelik, T.; Kolb, U. ‘‘Ab initio’’ structure solution from electron diffraction data obtained by a combination of automated diffraction tomography and precession technique. *Ultramicroscopy* **2009**, *109*, 758–765.
40. Zhang, D.; Oleynikov, P.; Hovmöller, S.; Zou, X. Collecting 3D electron diffraction data by the rotation method. *Z. Kristallogr.* **2010**, *225*, 94–102.
41. Kolb, U.; Mugnaioli, E.; Gorelik, T. E. Automated electron diffraction tomography – a new tool for nano crystal structure analysis. *Cryst. Res. Technol.* **2011**, *46*, 542–554.
42. Gemmi, M.; Oleynikov, P. Scanning reciprocal space for solving unknown structures: energy filtered diffraction tomography and rotation diffraction tomography methods. *Z. Kristallogr.* **2013**, *228*, 51–58.
43. Nannenga, B. L.; Shi, D.; Leslie, A. G. W.; Gonen, T. High-resolution structure determination by continuous-rotation data collection in MicroED. *Nat. Methods* **2014**, *11*, 927–930.
44. Gemmi, M.; La Placa, M. G. I.; Galanis, A. S.; Rauch E. F.; Nicolopoulos, S. Fast electron diffraction tomography. *J. Appl. Crystallogr.* **2015**, *48*, 718–727.
45. Rozhdestvenskaya, I. V.; Mugnaioli, E.; Schowalter, M.; Schmidt, M. U.; Czank, M.; Depmeier, W.; Rosenauer, A. The structure of denisovite, a fibrous nanocrystalline polytypic disordered ’very complex’ silicate, studied by a synergistic multi-disciplinary approach employing methods of electron crystallography and X-ray powder diffraction. *IUCrJ* **2017**, *4*, 223–242.
46. Jiang, J.; Jorda, J. L.; Yu, J.; Baumes, L. A.; Mugnaioli, E.; Diaz-Cabanas, M. J.; Kolb, U.; Corma, A. Synthesis and Structure Determination of the Hierarchical Meso-Microporous Zeolite ITQ-43. *Science* **2011**, *333*, 1131–1134.
47. Guo, P.; Shin, J.; Greenaway, A. G.; Min, J. G.; Su, J.; Choi, H. J.; Liu, L.; Cox, P. A.; Hong, S. B.; Wright, P. A.; Zou, X. A zeolite family with expanding structural complexity and embedded isoreticular structures. *Nature* **2015**, *524*, 74–78.
48. van Genderen, E.; Clabbers, M. T. B.; Das, P. P.; Stewart, A.; Nederlof, I.; Barentsen, K. C.; Portillo, Q.; Pannu, N. S.; Nicolopoulos, S.; Gruene, T.; Abrahams, J. P. *Ab initio* structure determination of nanocrystals of organic pharmaceutical compounds by electron diffraction at room temperature using a Timepix quantum area direct electron detector. *Acta Crystallogr. A* **2016**, *72*, 236–242.
49. Yuan, S.; Qin, J.-S.; Xu, H.-Q.; Su, J.; Rossi, D.; Chen, Y.; Zhang, L.; Lollar, C.; Wang, Q.; Jiang, H.-L.; Son, D. H.; Xu, H.; Huang, Z.; Zou, X.; Zhou, H. C. [$Ti_8Zr_2O_{12}(COO)_{16}$] Cluster: An Ideal Inorganic Building Unit for Photoactive Metal−Organic Frameworks. *ACS Cent. Sci.* **2018**, *4*, 105–111.
50. Rodriguez, J. A.; Ivanova, M. I.; Sawaya, M. R.; Cascio, D.; Reyes, F. E.; Shi, D.; Sangwan, S.; Guenther, E. L.; Johnson, L. M.; Zhang, M.; Jiang, L.; Arbing, M. A.; Nannenga, B. L.; Hattne, J.; Whitelegge, J.; Brewster, A. S.; Messerschmidt, M.; Boutet, S.; Sauter, N. K.; Gonen, T.; Eisenberg, D. S. Structure of the toxic core of α-synuclein from invisible crystals. *Nature* **2015**, *525*, 486–490.
51. Birkel, C. S.; Mugnaioli, E.; Gorelik, T.; Kolb, U.; Panthöfer, M.; Tremel, W. Solution Synthesis of a New Thermoelectric $Zn_{1+x}Sb$ Nanophase and Its Structure Determination Using Automated Electron Diffraction Tomography. *J. Am. Chem. Soc.* **2010**, *132*, 9881–9889.
52. Sarakinou, E.; Mugnaioli, E.; Lioutas, C. B.; Vouroutzis, N.; Frangis, N.; Kolb, U.; Nikolopoulos, S. Structure characterization of hard materials by precession electron

diffraction and automatic diffraction tomography: 6H–SiC semiconductor and $Ni_{1+x}Te_1$ embedded nanodomains. *Semicond Sci. Tech.* **2012**, *27*, 105003.
53. Baraldi, A.; Buffagni, E.; Capelletti, R.; Mazzera, M.; Fasoli, M.; Lauria, A.; Moretti, F.; Vedda, A.; Gemmi M. Eu Incorporation into Sol−Gel Silica for Photonic Applications: Spectroscopic and TEM Evidences of α- Quartz and Eu Pyrosilicate Nanocrystal Growth. *J. Phys. Chem. C* **2013**, *117*, 26831–26848.
54. Andrusenko, I.; Krysiak, Y.; Mugnaioli, E.; Gorelik, T. E.; Nihtianova, D.; Kolb, U. Structural insights into M_2O–Al_2O_3–WO_3 (M = Na, K) system by electron diffraction tomography. *Acta Crystallogr. B* **2012**, *71*, 349–357.
55. Mugnaioli, E.; Gemmi, M.; Merlini, M. and Gregorkiewitz M. $(Na,□)_5[MnO_2]_{13}$ nanorods: a new tunnel structure for electrode materials determined *ab initio* and refined through a combination of electron and synchrotron diffraction data. *Acta Crystallogr. B* **2016**, *72*, 893–903.
56. Nederlof, I.; van Genderen, E.; Li, Y.-W.; Abrahams, J. P. A Medipix quantum area detector allows rotation electron diffraction data collection from submicrometre three-dimensional protein crystals. *Acta Crystallogr. D* **2013**, *69*, 1223–1230.
57. Vincent, R.; Midgley, P. A. Double conical beam-rocking system for measurement of integrated electron diffraction intensities. *Ultramicroscopy* **1994**, *53*, 271–282.
58. Burla, M.C.; Caliandro, R.; Carrozzini, B.; Cascarano, G.L.; Cuocci, C.; Giacovazzo, C.; Mallamo, M.; Mazzone, A.; Polidori, G. Crystal structure determination and refinement *via SIR2014*. *J. Appl. Crystallogr.* **2015**, *48*, 306–309.
59. Sheldrick, G. M. A short history of *SHELX*. *Acta Crystallogr. A* **2008**, *64*, 112–122.
60. Doyle, P. A.; Turner P. S. Relativistic Hartree-Fock X-ray and Electron Scattering Factors. *Acta Crystallogr. A* **1968**, *24*, 390–397.
61. Bertoni, G.; Grillo, V.; Brescia R.; Ke, X.; Bals, S.; Catellani, A.; Li, H. and Manna, L. Direct Determination of Polarity, Faceting, and Core Location in Colloidal Core/Shell Wurtzite Semiconductor Nanocrystals. *ACS Nano* **2012**, *6*, 6453–6461.
62. Grillo, V. and Rotunno, E. STEM_CELL: A software tool for electron microscopy: Part I—simulations. *Ultramicroscopy* **2013**, *125*, 97–111.
63. Forman S. A.; Peacock, M. A. Crystal structure of rickardite, $Cu_{4-x}Te_2$. *Am. Miner.* **1949**, *34*, 441–451.
64. Baranova, R. V.; Avilov, A. S.; Pinsker Z. G. Determination of the crystal structure of the hexagonal phase β^{III} in the copper-tellurium system by electron diffraction. *Soviet Physics Crystallopraphy* **1974**, *18*, 736–740.
65. Blachnik, R.; Lasocka, M.; Walbrecht, U. The system copper-tellurium. *J. Solid State Chem.* **1983**, *48*, 431–438.
66. Pertlik, F. Vulcanite, CuTe: hydrothermal synthesis and crystal structure refinement. *Mineral. Petrol.* **2001**, *71*, 149–154.
67. Bindi, L.; Carbone, C.; Belmonte, D.; Cabella, R.; Bracco R. Weissite from Gambatesa mine, Val Graveglia, Liguria, Italy: occurrence, composition and determination of the crystal structure. *Miner. Mag.* **2013**, *77*, 475–483.

Acknowledgements

The authors thank JEOL Ltd. for the support in the HAADF-STEM and EDS mapping experiments at the EM Application Department in Tokyo, Japan. The authors acknowledge the Regione Toscana for funding the purchase of the Timepix detector through the FELIX project (Por CREO FESR 2014-2020 action).

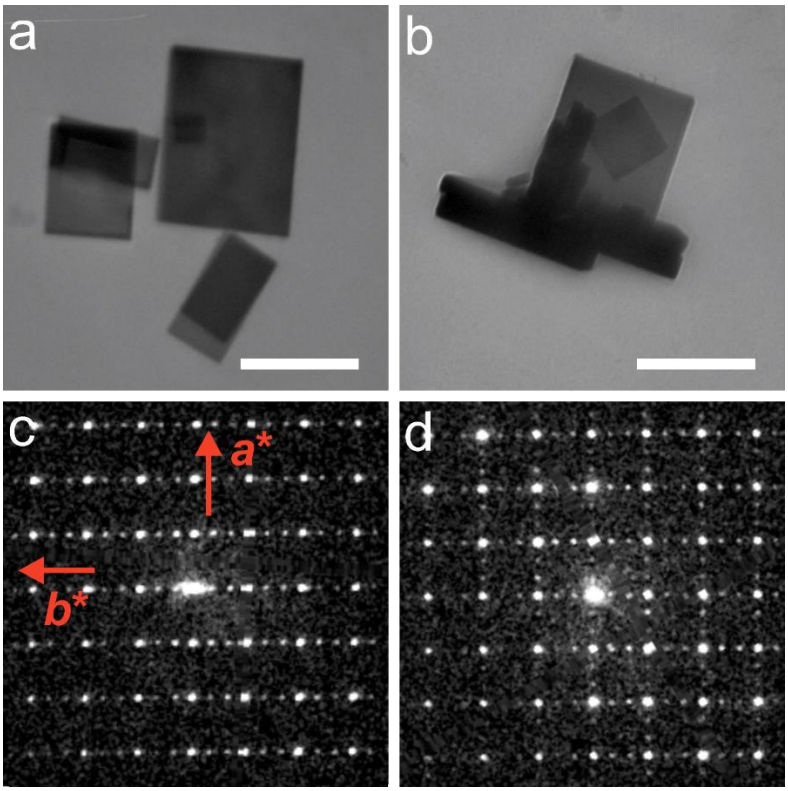
a
b
c
a*
b*
d

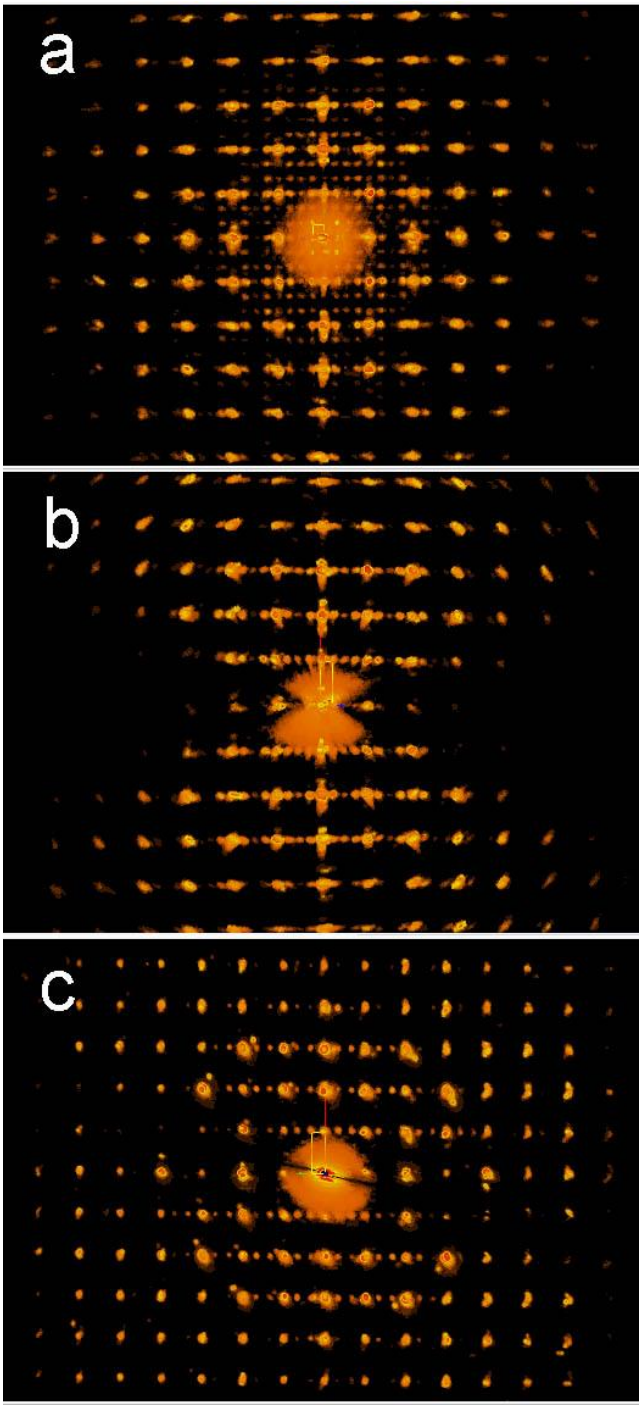
a
b
c

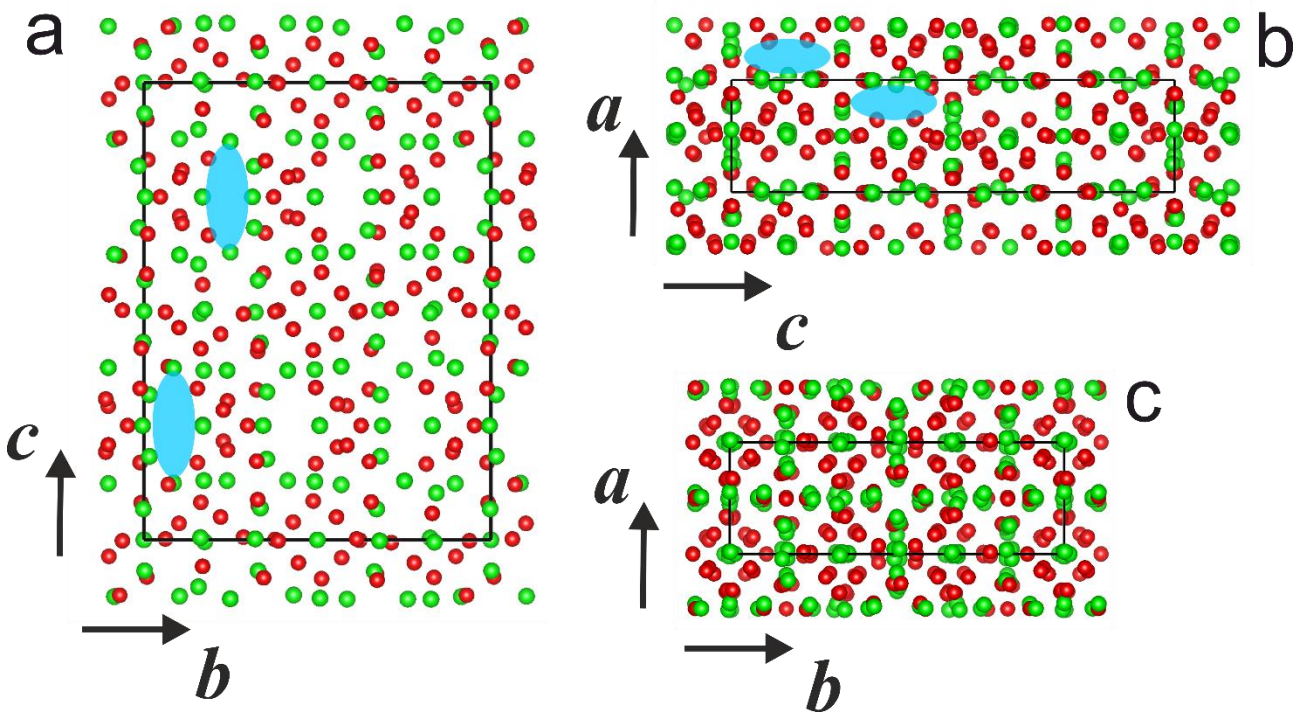
a
c
b
b
a
c
c
a
b

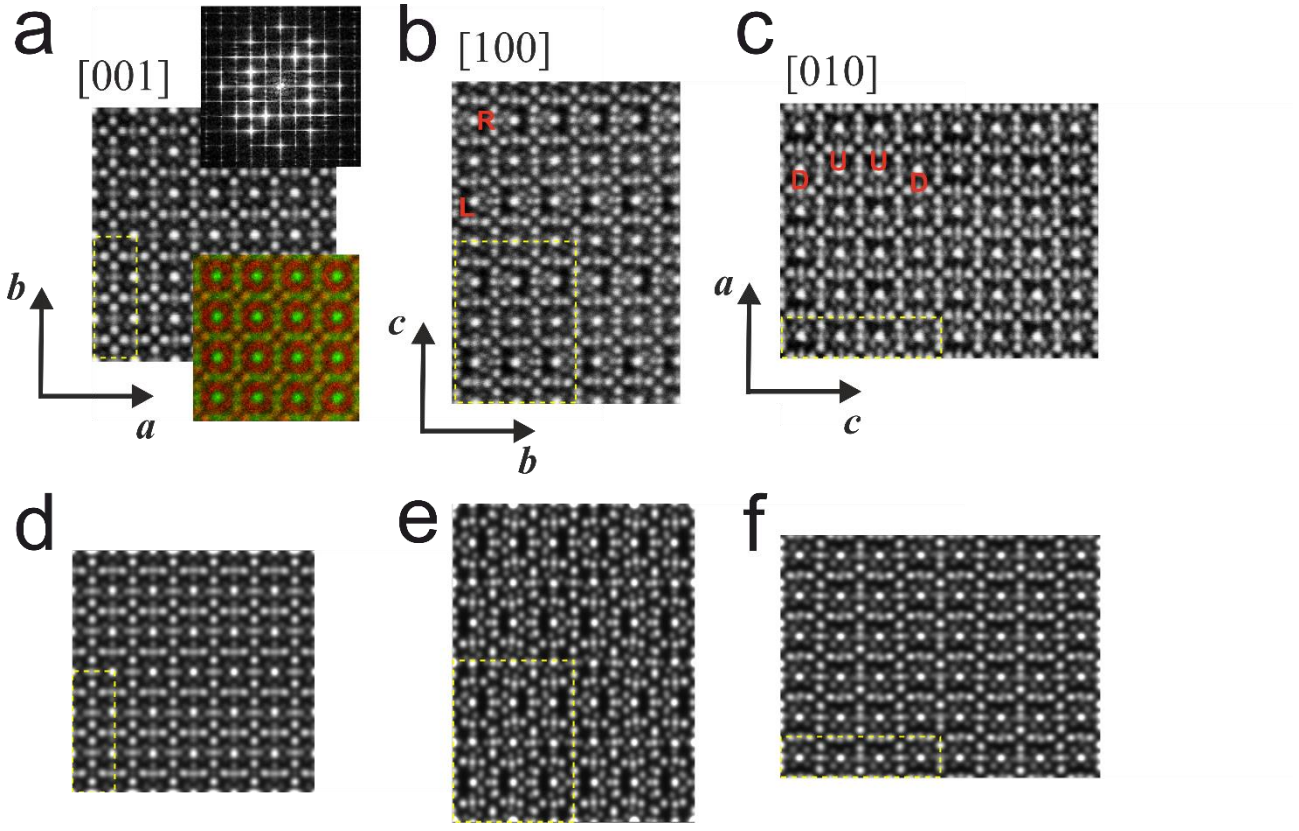
a
[001]
b
a
b
[100]
R
L
c
b
c
[010]
D
U
U
D
a
c

d
e
f

Figure 1. $Cu_{1.5}Te$ nanosheets (NS). (a) Low resolution TEM image of typical NSs lying on their large facet. Smaller NSs have generally a more elongated rectangular shape, while larger ones are more quadratic. (b) TEM image showing few $Cu_{1.5}Te$ NSs standing on side. The thickness of these NSs is around 30-40 nm. (c) Oriented [001] nano-beam diffraction pattern of a small rectangular NS, showing only one modulation-3 (crystallographic direction *b**). (d) Oriented [001] nano-beam diffraction pattern of a larger quadratic NS, showing two modulations-3 due to the pseudo-tetragonal twinning. Scale bar in (a) and (b) is 200 nm.

Figure 2. 3D EDT reconstructed diffraction volume for a single $Cu_{1.5}Te$ nanoparticle. (a) View along ***a**** showing both modulation-3 and modulation-4. (b) View along ***b**** showing only modulation-4. (c) View along ***c**** showing only modulation-3. Note that those are not conventional 2D oriented diffraction patterns, but projections of a 3D diffraction volume.

Figure 3. $Cu_{1.5}Te$ structure determined and refined by electron diffraction tomography (EDT) data. (a) View along [100], with [100] channels highlighted in blue. (b) View along [010]. Projections of low-density regions responsible for the up-up-down-down pattern in [010] HAADF-STEM images are highlighted in blue. (c) View along [001].

Figure 4. Experimental and simulated HAADF-STEM images of NSs. (a) Experimental image taken along [001]. The upper inset shows the corresponding FFT, where the modulation-3 is more evident. The lower inset shows the EDS chemical map at atomic resolution, where the Te sublattice (green) and the Cu sublattice (red) are straightforwardly addressed. (b) Experimental image taken along [100]. The typical left-null-right-null Cu vacancy pattern along *c* is emphasized by red labels (L and R). (c) Experimental image taken along [010]. The down-up-up-down Cu vacancy pattern along *c* is emphasized by red labels (D and U). (d) Simulated image along [001]. (e) Simulated image along [100]. (f) Simulated image along [010]. Unit cell is sketched in yellow.

Table of Contents Synopsis

We investigated pseudo-cubic $Cu_{2-x}Te$ nanosheets using electron diffraction tomography and high-resolution HAADF-STEM imaging. The structure of this metastable nanomaterial was determined *ab initio* by 3D electron diffraction data recorded by a new generation background-free single-electron detector. The presence of two different, crystallographically defined modulations creates a 3D connected vacancy channel system, which accounts for the strong localized surface plasmon resonance in the near-infrared region of this material.

Table of Contents Graphic